



**HAL**  
open science

## Temperature Rise Caused by Shear Wave Elastography, Pulse Doppler and B-Mode in Biological Tissue: An Infrared Thermographic Approach

Maha Issaoui, Xavier Balandraud, Michel Grédiac, Benoit Blaysat, Lemlih Ouchchane, Amelie Delabaere, Marie-Pierre Sauvant-Rochat, Didier Lemery

► **To cite this version:**

Maha Issaoui, Xavier Balandraud, Michel Grédiac, Benoit Blaysat, Lemlih Ouchchane, et al.. Temperature Rise Caused by Shear Wave Elastography, Pulse Doppler and B-Mode in Biological Tissue: An Infrared Thermographic Approach. *Ultrasound in Medicine & Biology*, 2020, 46 (2), pp.325-335. 10.1016/j.ultrasmedbio.2019.10.008 . hal-04004981

**HAL Id: hal-04004981**

**<https://uca.hal.science/hal-04004981>**

Submitted on 25 Feb 2023

**HAL** is a multi-disciplinary open access archive for the deposit and dissemination of scientific research documents, whether they are published or not. The documents may come from teaching and research institutions in France or abroad, or from public or private research centers.

L'archive ouverte pluridisciplinaire **HAL**, est destinée au dépôt et à la diffusion de documents scientifiques de niveau recherche, publiés ou non, émanant des établissements d'enseignement et de recherche français ou étrangers, des laboratoires publics ou privés.

1 **Temperature rise caused by Shear Wave Elastography,**  
2 **Pulse-Doppler and B-mode in biological tissue: an infrared**  
3 **thermographic approach**

4  
5 Maha Issaoui<sup>a</sup>, Xavier Balandraud<sup>a</sup>, Michel Grédiac<sup>a</sup>, Benoit Blaysat<sup>a</sup>, Lemlih Ouchchane<sup>b,c</sup>,  
6 Amelie Delabaere<sup>b,d</sup>, Marie-Pierre Sauvant-Rochat<sup>a,e</sup>, and Didier Lemery<sup>b,d</sup>

7  
8 <sup>a</sup> Université Clermont Auvergne, CNRS, SIGMA Clermont, Institut Pascal, F-63000  
9 Clermont-Ferrand, France

10 <sup>b</sup> Université Clermont Auvergne, CHU Clermont-Ferrand, CNRS, SIGMA Clermont, Institut  
11 Pascal, F-63000 Clermont-Ferrand, France

12 <sup>c</sup> Département de Santé Publique, Unité de Biostatistique et Informatique Médicale, CHU de  
13 Clermont-Ferrand, F-63000 Clermont-Ferrand, France

14 <sup>d</sup> Pôle Femme et Enfant, Centre Hospitalier Universitaire de Clermont-Ferrand, F-63000  
15 Clermont-Ferrand, France

16 <sup>e</sup> Département de Santé Publique et Environnement, Université Clermont-Auvergne, UFR  
17 Pharmacie, F-63000 Clermont-Ferrand, France.

18  
19 Address correspondence to: Maha Issaoui, Université Clermont Auvergne, CNRS, SIGMA  
20 Clermont, Institut Pascal, F-63000 Clermont-Ferrand, France. E-mail:

21 [maha.issaoui@etu.uca.fr](mailto:maha.issaoui@etu.uca.fr)

22

23 **Abstract**—The aim of the study is to demonstrate the interest and relevance of infrared  
24 thermography, which is a non-invasive full-field surface temperature measurement technique,  
25 to characterize the heterogeneous heating caused by ultrasound in biological tissue. Thermal  
26 effects of Shear Wave Elastography (SWE), Pulse-Doppler (PD) and B-mode were evidenced  
27 in porcine tissue. Experiments were performed using a high-frequency echography  
28 Aixplorer® system (Supersonic Imagine, Aix-en-Provence, France). For the three modes,  
29 ultrasound was applied continuously for 360 seconds while the temperature was recorded at  
30 the sample surface with a Cedip Jade III-MWIR infrared camera (Flir, Torcy, France).  
31 Temperature changes were detected for the three modes. In particular, “heat tunnels” crossing  
32 the sample were visualized from the early stages of the experiment. Heat conduction from the  
33 transducer was also involved in the global warming of the sample. The maximum heating  
34 induced by SWE was almost 1.6 degrees Celsius, whereas it was 0.7 and 0.6 degrees Celsius  
35 for PD and B-mode respectively. The study opens up prospects for safety studies, potentially  
36 in addition to classical approaches such as those using thermocouples.

37

38 **Keyword:** Shear Wave Elastography; Ultrasound; Infrared thermography; Temperature rise;  
39 Safety

40

41

42

## INTRODUCTION

43

44 Shear Wave Elastography (SWE) exploits acoustic radiation force (ARF) to generate stiffness  
45 maps in biological tissue. In practice, a 100  $\mu$ s focused compression wave generates radiation  
46 force in dissipative biological media, which pushes the tissue for some dozens of  $\mu$ m in the  
47 target focal zone. When the tissue relaxes, it creates a shear wave propagating perpendicularly  
48 to the axis of the ultrasound beam at a speed of about 1 m/s. This shear wave is then  
49 visualized by ultrafast ultrasound imaging, capturing the wave front every 10 ms. Shear wave  
50 propagation speed is related to the Young's modulus of the biological tissue, a physical  
51 property usually expressed in kPa and characterizing material stiffness (Gennisson et al.  
52 2013). The clinical relevance of SWE has been demonstrated for the detection of masses in  
53 superficial organs such as breast cancer (Cosgrove et al. 2012), and for the diagnosis of  
54 pathologies in deep organs, such as a cirrhotic liver (Guibal et al. 2016).

55 With the increasing number of publications on elastography, the World Federation for  
56 Ultrasound in Medicine and Biology (WFUMB) decided to take the initiative to create  
57 guidelines in August 2011. The first consensus meeting was held in March 2013 and led to the  
58 development of guidelines for basic science in elastography (Shiina et al. 2015), and for the  
59 use of this technique for the breast (Barr et al. 2015) and liver (Ferraioli et al. 2015), without  
60 distinguishing between the different elastography modes.

61 Elastography has recently been applied to gynecology (Thomas et al. 2007; Ami et al.  
62 2009) and obstetrics (Kiliç et al. 2015; Alan et al. 2016; Quarello et al. 2016). Many  
63 published articles already deal with tissues that are accessible to methods necessitating the  
64 direct compression of the organ by the ultrasound probe, such as the cervix (Molina et al.  
65 2012; Khalil et al. 2013; Hernandez-Andrade et al. 2014; Fruscalzo et al. 2016; O'Hara et al.

66 2018). Since SWE enables imaging without direct contact between the transducer and the  
67 observed tissue, it appears as the ideal candidate for fetal tissue elastography examinations  
68 (Diguisto et al. 2017; Mottet et al. 2017). However, until now there have been no guidelines  
69 on the use of SWE in obstetrics. Regardless of its clinical relevance, it is necessary to  
70 demonstrate its safety before allowing its utilization in routine practice for fetuses.

71         Ultrasound can lead to two main types of potential effects on biological tissues,  
72 namely thermal and mechanical effects (Shankar and Pagel 2011a). The thermal effect was  
73 for instance studied by Palmeri and Nightingale (2004) using thermocouples placed inside the  
74 tissue (Palmeri et Nightingale 2004). It is important to note that the period of organogenesis is  
75 considered as particularly sensitive to thermal stress (Fowlkes 2008). Investigations on  
76 laboratory animals have documented that an elevation in temperature can damage biological  
77 tissues (Pellicer et al. 2011; Schneider-Kolsky et al. 2009). Thermally-induced teratogenesis  
78 has been shown in many animal studies (Germain et al.1985). The issue of temperature rise  
79 due to ultrasound, and SWE in particular, is thus critical.

80         In the present work, we focus on the observation of the thermal effect in biological  
81 tissue generated by three ultrasonic modes, namely SWE, Pulse-Doppler (PD) and B-mode.  
82 An infrared (IR) thermographic camera was used for this purpose. This device provides full-  
83 field temperature measurements at the surface of the object under investigation. In the last few  
84 decades, IR thermography has become widespread in the mechanics of materials community,  
85 leading to important insights into the thermal response of materials subjected to mechanical  
86 solicitation (Chrysochoos et al. 2010). It is in particular possible to experimentally evidence  
87 thermo-mechanical couplings, i.e. temperature variations caused by changes in the mechanical  
88 state of the material. Various mechanical phenomena in various materials are related to  
89 calorific responses, for instance elasticity, plasticity, viscosity, fatigue damage, elasto-plastic  
90 transition, cracking, vibrations, friction, strain- or stress-induced phase transitions, etc. IR

91 thermography is now recognized as a relevant experimental means to study the  
92 thermomechanics of materials. However, to the best of the authors' knowledge,  
93 thermographic approaches have not before been applied to the calorific response of biological  
94 tissues subjected to ultrasound solicitation.

95         The aim of the present study is to demonstrate the interest and the relevance of IR  
96 thermography to characterize the heterogeneous heating caused by ultrasound in biological  
97 tissue. Two modalities which are already authorized for pregnant women (PD and B-mode)  
98 were compared with the SWE mode, with potential perspectives for the study of the safety of  
99 the latter in obstetrics (Issaoui et al. 2018).

100

101

## MATERIALS AND METHODS

102

### *Experimental setup*

104

105         The echography system used for the experiments was a high-frequency Aixplorer®  
106 (Supersonic Imagine, Aix-en-Provence, France). It features three imagery modes: B-Mode,  
107 PD and SWE. The chosen transducer, typically used in obstetrics, was a curved SC6-1 probe  
108 (Supersonic Imagine, Aix-en-Provence, France) featuring 192 piezoelectric elements and a  
109 bandwidth of 1-6 MHz. Temperature measurements were carried out using a Cedip Jade III-  
110 MWIR camera (Flir, Torcy, France). This IR camera features a wavelength range of 3.5-5  $\mu\text{m}$ ,  
111 a sensor size of 320×240 pixels and a Noise Equivalent Temperature Difference (NETD)  
112 equal to 0.02°C. This latter quantity can be assimilated to the temperature measurement  
113 resolution, that is, the change in quantity being measured that causes a change in the  
114 corresponding indication of greater than one standard deviation of the measurement noise

115 (Chrysochoos and Surrel 2012). The lower the measurement resolution, the lower the noise  
116 and thus the better the measurement.

117 Measurements were performed on homogeneous pieces of porcine tissue  
118 (slaughterhouse: Hassenforder et fils S.A.S., Vichy, France; identification number: 11P18025;  
119 FR-03-094-001 CE; order number; CV18032542) by three operators (MI, XB and DL).  
120 Several samples with dimensions of  $130 \times 50 \times 60 \text{ mm}^3$  were cut by hand. Two configurations  
121 were tested in terms of the location of the transducer with respect to the porcine sample (Fig.  
122 1-a). The reason for this positioning on the sample was that IR thermography provides  
123 temperature maps at the surface of the observed object. In Configuration #1, the surface  
124 observed by the IR camera is perpendicular to the plane of the transducer, whereas it is  
125 parallel to it in Configuration #2. The two test configurations were considered as  
126 complementary in order to obtain two perpendicular slices of the three-dimensional  
127 temperature field in the bulk.

128 A second sample was used as a reference to track thermal fluctuations in the close  
129 environment (Fig. 1-b). The sample to be subjected to ultrasound (named “sample” in the  
130 following) and the reference sample (named “reference” in the following) were placed in a  
131 homemade plastic frame featuring two shelves. The reference was placed under the sample, in  
132 the IR camera’s field of view. The bottom part of the transducer was also visible at the top of  
133 the thermal images. Note that the reference was placed close enough to the sample so that it  
134 can be reasonably assumed that it was submitted to the same environmental fluctuations  
135 during testing. However, the reference was physically separate from the sample, so it was not  
136 affected by ultrasonic solicitations.

137 Figure 1-c shows three photographs of the experiment. The transducer was in contact  
138 with the sample using a static system ensuring a constant force. The sample was therefore  
139 deformed in addition to the effect of gravity. It is worth noting that performing quantitative

140 measurements with an IR camera is somewhat tricky when temperature changes are small.  
141 This is due to the fact that various phenomena potentially influence the measured  
142 temperatures in addition to the desired ones, for instance potential changes in the ambient  
143 airflow or in ambient temperature, and more generally in the elements inside the testing room  
144 (persons, heating system, doors opened, etc.). Misleading conclusion could therefore be  
145 drawn from measured temperature fields if some precautions are not taken when preparing  
146 and performing the tests. First, a cardboard tunnel was placed between the IR camera and the  
147 observed surfaces. Second, attention was paid to ensure the steady thermal state of the testing  
148 room. To this end, the echography system, IR camera and computers were turned on three  
149 hours before the test session began, and nobody was present in the room during the tests, in  
150 order to limit airflow.

151         The three echography modes (B-mode, PD and SWE) were applied for comparison  
152 purposes. For the three modes, the ultrasonic solicitation ran continuously for 360 s and then  
153 stopped. For each test, the IR camera measurements lasted longer than this, so that  
154 temperature variations could be monitored after the ultrasonic activity had stopped. A waiting  
155 time of one hour was respected between two consecutive tests, to ensure a thermal steady  
156 state when starting the second one. Note that for the B-mode, two focalization configurations  
157 were also compared (10-25 mm and 25-40 mm), but preliminary tests showed that there was  
158 no difference in terms of temperature distributions. Finally, the spatial resolution of the  
159 measured temperature maps was 0.53 mm. From a metrological point of view, the spatial  
160 resolution of the measured fields can be defined as the shortest distance between two spatially  
161 independent measurements. The IR camera used here features independent sensors, so the  
162 spatial resolution is equal to the pixel size projected on the surface under investigation. Each  
163 temperature map can thus be seen as a grid of “thermocouples” with a pitch equal to 0.53 mm.  
164



165 *Measurement of temperature change due to ultrasonic solicitation*

166

167 Two precautions were taken to ensure the correct assessment of the temperature  
168 changes due to ultrasound: (i) the use of specific thermal acquisition conditions to reduce  
169 noise, and (ii) the subtraction of thermal fluctuations in the environment thanks to the  
170 reference.

171 (i) The IR camera acquisition frequency  $f_A$  was set to 100 Hz, but each recorded  
172 image was the average of 50 successive frames, thus leading to a recording frequency  $f_R$  of  
173 2 Hz. This setting was chosen based on preliminary tests (not detailed here) which showed  
174 that the temperature change is smooth enough whatever echography mode is chosen. Indeed,  
175 no “sudden” temperature increase could be observed. Averaging enables us to improve the  
176 measurement resolution compared to the base NETD of the IR camera, but without losing  
177 information. In theory, for Gaussian noise, the temporal averaging operation of 50 frames  
178 improves the measurement resolution by a factor of  $\sqrt{50}$  but this impairs the temporal  
179 resolution. Applying this procedure leads the standard deviation of the resulting noise to be  
180 equal to some thousandths of one degree only.

181 (ii) Figure 2 illustrates the interest of using the reference for the correct assessment of  
182 the temperature change due to ultrasound only. The data correspond here to a test performed  
183 in Configuration #1 for the B-mode. The black curve shows the temperature change of the  
184 reference, while the blue one shows the temperature at point A on the sample subjected to  
185 ultrasound (see schematic view in Figure 2 for the location of point A). Note that the  
186 measurement resolution of the reference temperature was improved by spatially averaging  
187 over a large rectangular zone (see schematic view in Figure 2). The red curve corresponds to  
188 the temperature change at point A due to ultrasonic waves only, obtained by subtracting the  
189 temperature change of the reference from that of the sample. Even if fluctuations in the

190 environment (black curve) were limited to a few hundredths of a degree, it can be seen that  
191 the raw data at point A slightly underestimates the data to be considered for the analysis (the  
192 blue curve is below the red one). It is worth noting that the “strong” parasitic perturbation  
193 around time 120 s was correctly removed by the processing.

194

195

## RESULTS

196

197 For the sake of legibility, physical measurements are commented in the present section while  
198 the clinical impact is developed in the following one.

199

### *Analysis of some temperature change maps*

201

202 Figure 3 presents the maps of temperature change at  $t = 80$  s in Configuration #1 for  
203 the three echography modes. This specific time was selected to highlight the *remote* heating  
204 from the transducer. The following comments can be drawn from this figure:

- 205 • for the three modes, a vertical “heat tunnel” is visible under the contact with the  
206 transducer (see the arrows in the images). This phenomenon cannot be explained by an  
207 increase in the transducer temperature accompanied by heat conduction inside the  
208 sample. Indeed, assuming isotropic thermal conduction in the tissue, a concentric  
209 distribution would have been obtained if only heat conduction was involved;
- 210 • the vertical tunnels appear to be quite homogeneous in temperature for both the B-  
211 mode (Fig. 3-a) and PD (Fig. 3-b), whereas hotter zones are clearly visible at the  
212 bottom part and some centimeters under the contact with the transducer for SWE (Fig.  
213 3-c). This latter observation confirms the *remote* heating from the transducer, which is  
214 due to the ultrasonic waves crossing the sample in the plane of the transducer. The hot

215 zone at the bottom part can be explained by a reflection of the waves, whereas the hot  
216 zone under the contact with the transducer can be explained by an effect of wave  
217 focalization;

- 218 • in order to have better color dynamics for each mode individually, Figure 3-d shows  
219 some close-up views of the central zone with suitable color scales. With these  
220 representations, reflections at the bottom part of the sample are also visible for the B-  
221 mode. Clearly, SWE is calorically greater than both B-mode and PD.

222 As a general conclusion from Figure 3, the three heat tunnels in the temperature change maps  
223 constitute a clear signature of remote heating from the transducer, associated with wave  
224 propagation.

225 Figure 4 presents the thermal maps obtained for Configuration #1 at the end of  
226 transducer activation, i.e. at  $t = 360$  s. For B-mode and PD (Figs. 4-a and -b), the color scales  
227 are the same as in Figure 3, for comparison purposes. For SWE, the color scale was modified  
228 because of the much stronger thermal activity for this mode. As a first comment, the heat  
229 tunnels can again be observed, but they appear thicker compared to those obtained at  $t = 80$  s  
230 (Fig. 3). Moreover, their widths are not homogeneous: they are indeed larger at their ends  
231 (close to the transducer and at the bottom). This can be explained by heat conduction inside  
232 the tissue: the heat that was created *remotely* by the waves progressively diffused. As a  
233 general comment, temperature distribution is the result of three causes: the heat source  
234 produced by wave propagation, heat conduction inside the tissue, and the heat exchanged with  
235 the sample environment (by convection with ambient air and by contact with both the frame  
236 and the transducer).

237 Figure 5 presents the temperature change maps for  $t = 360$  s for Configuration #2 and  
238 for the three echography modes. The magnitude of temperature increase is globally greater  
239 than for Configuration #1 at the same time (see Figure 4). The link between the data for the

240 two configurations will be discussed in the next section. In the measurement plane observed  
241 with Configuration #2, the highest temperature changes in the sample are located close to the  
242 transducer, which can be explained by heat transfer through contact. Heat tunnels similar to  
243 those observed for Configuration #1 are visible, although they are more difficult to visualize  
244 (dark blue).

245 It is worth noting that such features can only be observed and quantified thanks to a  
246 full-field thermal measurement technique.

247

### 248 *Analysis of the temperature time variation*

249

250 Figure 6 shows the temperature change as a function of time at two points A and B, for  
251 Configurations #1 and #2 respectively, for the three echography modes. The locations of these  
252 points were chosen because they correspond to the most intense heating zones. The vertical  
253 dashed lines correspond to the end of transducer activation, i.e. at time  $t = 360$  s. Several  
254 comments can be made with respect to this figure:

- 255 • SWE generates greater temperature changes for both configurations. PD causes a  
256 larger increase in temperature than B-mode. This result is in agreement with previous  
257 studies, see Ref. (Miloró et al. 2017) for instance;
- 258 • for Configuration #2, the temperature clearly still increases for several tenths of a  
259 second after halting the ultrasonic solicitation (Fig. 6-b). This phenomenon can be  
260 explained by the fact that heat is still transferred from the “hot” transducer. This  
261 confirms that, in addition to *remote* heating, heat conduction is also involved;
- 262 • as indicated in the “Materials and methods” section, Configurations #1 and #2 were  
263 initially considered as complementary, to obtain two perpendicular slices of the tri-  
264 dimensional temperature field in the bulk. This hypothesis appears to be reasonable

265 when comparing Figures 6-a and 7. The latter presents the temperature change as a  
266 function of time for another point (named C) in Configuration #2. This point is at the  
267 same location with respect to the transducer as point A in Configuration #1: see the  
268 schematic view at the top of Figure 7. At time  $t = 360$  s for the B-mode, the  
269 temperature increase is nearly equal to  $0.3^{\circ}\text{C}$  for both Configurations #1 and #2  
270 (compare the green curves in Figures 6-a and 7). Similarly, the temperature increase  
271 for PD at  $t = 360$  s is nearly equal to  $0.4^{\circ}\text{C}$  for both configurations (compare the blue  
272 curves in Figures 6-a and 7);

273 • a specific remark can be made concerning the SWE mode. At  $t = 360$  s, the  
274 temperature change is nearly equal to  $1.15^{\circ}\text{C}$  for both configurations (compare the red  
275 curves in Figures 6-a and 7), but the temperature continues to increase in  
276 Configuration #2 after  $t = 360$  s, reaching  $1.56^{\circ}\text{C}$ . This result can be explained by the  
277 fact that points A and C are not exactly equivalent. For instance, it can be noted that  
278 the hatched zone in Configuration #2 is not present in Configuration #1 (Fig. 7). This  
279 effect of thermal inertia is also visible in Figure 7 for both PD and B-mode, even if it  
280 is less pronounced than for SWE.

281

282 Finally, Figures 8, 9 and 10 provide the temperature change as a function of time for the B-  
283 mode, PD and SWE respectively, at various points and for both configurations. The location  
284 of these points is reported in Figure 8-a for Configuration #1 and in Figure 8-b for  
285 Configuration #2. Point P1 corresponds to point A in Figure 6-a (Configuration #1), while  
286 Point P8 corresponds to point B in Figure 6-b (Configuration #2). An additional point (P0)  
287 was directly placed on the transducer in Configuration #2, enabling us to capture the highest  
288 temperature change in the thermal scene. It can be observed that, at the end of the ultrasonic  
289 solicitation (at  $t = 360$  s), the temperature of the transducer reaches  $0.95^{\circ}\text{C}$  for the B-mode

290 and PD, and 1.95°C for SWE. Close to the transducer, heat conduction by contact is not  
291 negligible. Note that the noise in the curves in Figures 8-a (B-mode in Configuration #1) and  
292 9-a (PD in Configuration #1) appears to be greater than in the other curves, merely because of  
293 the scale used for the y-axis. As already noted above, B-mode and PD are less calorific than  
294 SWE.

295

296

## DISCUSSION

297

298 Elastography, including SWE, is commonly used in various clinical applications (Cosgrove et  
299 al. 2012; Guibal et al. 2016). Potential indications of SWE in fetal and uterine imaging during  
300 pregnancy are cervix examination (Fruscalzo et al. 2016), and more importantly the  
301 monitoring of fetal development. Recently, SWE was used to explore the fetal brain (Diguisto  
302 et al. 2017) and lung (Mottet et al. 2017). In these studies, the authors considered that the  
303 benefit-to-risk ratio of this technique was favorable. However, a recent review was unable to  
304 demonstrate the safety of SWE regarding the fetus (Issaoui et al. 2018). Palmeri and  
305 Nightingale (2004), Nitta et al. (2001) and Bouchard et al. (2009) studied the temperature rise  
306 created by ARF in soft tissue (porcine muscle) by using thermocouples (Palmeri et  
307 Nightingale 2004; Bouchard et al. 2009; Nitta et al. 2015). Skurczynski et al. (2009) analyzed  
308 the temperature increase and the cavitation effect by performing focused ultrasound: they  
309 reported a potential heating risk during elasticity measurement by ARF when a bone is  
310 present (Skurczynski et al. 2009). The effect of temperature rise potentially leading to the  
311 teratogenesis of developing tissues was evidenced *in vivo* in animal models. This effect is  
312 documented in Refs (Hinoue et al. 2001; Church and Miller 2007; Abramowicz et al. 2008;  
313 Shankar and Pagel 2011b). Abnormalities include growth retardation, microencephaly,  
314 cataract, and other malformations (Ziskin and Morrissey 2011). Some *in vivo* experiments

315 have also shown that the threshold temperature increase for teratogenic effects induced by  
316 hyperthermia is estimated at 1.5°C for an exposure of 5 min (Abramowicz 2002; Abramowicz  
317 et al. 2008). A major problem with formulating hypotheses from animal data is that *in vivo*  
318 effects of hyperthermia seen in animals result from exposure situations that would never be  
319 encountered by the human embryo or fetus during ultrasound examination. However, a review  
320 of the literature by Marinac-Dabic et al. (2002) identified the epidemiologic studies focusing  
321 on human exposure to diagnostic ultrasound during pregnancy (Marinac-Dabic et al. 2002)  
322 and the potential associations between *in utero* ultrasound exposure and growth restriction,  
323 delayed speech, dyslexia and non-right-handedness. The authors concluded that there was no  
324 association between *in utero* exposure to ultrasound and either growth restriction or delayed  
325 speech. There are, nonetheless, some questions about non-right-handedness after frequent  
326 exposure to Doppler ultrasound. However, no definitive conclusions can yet be drawn. To  
327 date no study has specifically looked at the effects of SWE.

328         In this context, developing experimental techniques to measure the temperature rise in  
329 biological tissue caused by ultrasound is of prime interest. Thermocouples placed inside the  
330 tissue are classically employed and have proved to be efficient. The present study shows that  
331 IR thermography could be a complementary experimental approach. This technique provides  
332 temperature maps without contact with the tissue, thus avoiding the potential artefacts that  
333 thermocouples may cause. Indeed, since ARF creates a matter displacement, it is difficult to  
334 know to what extent a thermocouple will generate a secondary ultrasound source (thus  
335 creating a secondary heat source).

336         A limitation of our study is that it was performed on samples containing only soft  
337 tissues: our samples did not contain bone parts. Many other studies have shown that the  
338 thermo-sensitivity of bone is much higher than that of soft tissues (Skurezynski et al. 2009;  
339 Nitta et al. 2015; Tabaru et al. 2012). In fact, a fetus is composed principally of soft tissues

340 but also of bones. For obvious ethical reasons however, it was impossible to perform these  
341 tests on fetal tissues. Further studies should be performed on phantoms containing soft tissues  
342 and bones.

343 The strength of the present test campaign is that precautions were taken to avoid  
344 potential misinterpretation of the results: a waiting time before starting any new test from an  
345 initial thermal steady state, the subtraction of parasitic effects thanks to a reference sample,  
346 and noise reduction. It can be noted that, as usual for full-field measurement techniques, huge  
347 amounts of data were recorded (videos of several hundreds of Mb for each test) and  
348 processed. After preliminary tests, the experiments were repeated twice in order to check that  
349 the results were similar. Let us recall that the objective of the study was not to perform a  
350 statistical analysis of the results, but to demonstrate the relevance of IR thermography as an  
351 experimental tool for the study of temperature increases due to ultrasound use.

352 Some final comments can be advanced about the material used for the test. Porcine  
353 muscle was chosen because it has well-characterized acoustic and thermal properties, similar  
354 to those reported for clinically relevant human soft tissues (Liang et al. 1991). There are  
355 problems in relating laboratory animal studies to humans. We cannot extrapolate to humans  
356 the results of studies performed on animals, or even from one animal species to another,  
357 because differences in the results and conclusions may be due to strain differences. At this  
358 stage of our knowledge, we cannot confirm that SWE has an acceptable temperature increase,  
359 or that it could be considered as safe for the developing tissue of the fetus.

360

361

## CONCLUSION

362

363 SWE is a recent ultrasound modality offering the possibility of a quantitative assessment of  
364 tissue elasticity. It may have numerous potential applications in obstetric and fetal imaging.



365 The present study demonstrated the benefit of using surface temperature maps captured by an  
366 IR camera for the analysis of heterogeneous heating caused by ultrasound. The temperature  
367 rise in SWE mode appeared to be much higher compared to the other two modes under study  
368 (B-mode and PD), as has already been indicated in thermocouple-based studies. The IR  
369 thermography technique, in parallel with the thermocouple approach, could advantageously  
370 be employed to study the safety of SWE in obstetrics. Tests on samples containing both soft  
371 tissues and bones are also a perspective of this study. Finally, future works could also concern  
372 the coupling of IR thermography with thermocouples placed inside a phantom imitating  
373 biological tissue, in order to potentially reconstruct the variations in the entire three-  
374 dimensional temperature field accompanying ultrasound.

375

## 376 **ACKNOWLEDGEMENTS**

377

378 The authors would like to thank Dr. Piero Miloro from National Physical Laboratory (NPL),  
379 UK for the fruitful discussions about temperature rises due to elastography in tissues.

380

## 381 **REFERENCES**

382

383 Abramowicz JS. Ultrasound in obstetrics and gynecology: Is this hot technology too hot? J  
384 Ultrasound Med 2012;21(12):1327–33.

385 Abramowicz JS, Barnett SB, Duck FA, Edmonds PD, Hynynen KH, Ziskin MC. Fetal  
386 thermal effects of diagnostic ultrasound . J Ultrasound Med 2008;27(4):541–59.

387 Alan B, Goya C, Tunç S, Teke M, Hattapoğlu S. Assessment of placental stiffness using  
388 acoustic radiation force impulse elastography in pregnant women with fetal anomalies.

389 Korean J Radiol 2016;17(2):218–23.

390 Ami O, Lamazou F, Mabilille M, Levailant JM, Deffieux X, Frydman R, Musset D. Real-time  
391 transvaginal elastosonography of uterine fibroids. *Ultrasound Obstet Gynecol*  
392 2009;34(4):486–88.

393 Barr RG, Nakashima K, Amy D, Cosgrove D, Farrokh A, Schafer F, Bamber JC, Castera L,  
394 Choi BI, Chou YH, Dietrich CF, Ding H, Ferraioli G, Filice C, Friedrich-Rust M, Hall  
395 TJ, Nightingale KR, Palmeri ML, Shiina T, Suzuki S, Sporea I, Wilson S, Kudo M.  
396 WFUMB guidelines and recommendations for clinical use of ultrasound elastography:  
397 Part 2: breast. *Ultrasound Med Biol* 2015;41(5):1148–60.

398 Bouchard RR, Dahl JJ, Hsu SJ, Palmeri ML, Trahey GE. Image quality, tissue heating, and  
399 frame rate trade-offs in acoustic radiation force impulse imaging. *IEEE Trans Ultrason*  
400 *Ferroelectr Freq Control*. 2009;56(1):63–76.

401 Chrysochoos A, Huon V, Jourdan F, Muracciole JM, Peyroux R, Wattrisse B. Use of full-  
402 field digital image correlation and infrared thermography measurements for the  
403 thermomechanical analysis of material behaviour. *Strain* 2011;46(1):117–130

404 Chrysochoos A and Surrel Y. Basics of metrology and introduction to techniques. In: Grediac  
405 M and Hild F (Eds) *Full-field measurements and identification in solid mechanics*,  
406 Wiley-ISTE, 2012. pp. 1–29

407 Church CC and Miller WM. Quantification of risk from fetal exposure to diagnostic  
408 ultrasound. *Prog Biophys Mol Biol* 2007;93(1):331–53.

409 Cosgrove DO, Berg WA, Doré CJ, Skyba DM, Henry JP, Gay J, Cohen-Bacrie C. Shear wave  
410 elastography for breast masses is highly reproducible. *Eur Radiol* 2012;22(5):1023–32.

411 Diguisto C, Simon EG, Callé S, Ternifi R, Remeniéras JP, Hervé P, Perrotin F. Ultrasonic  
412 elastography exploration of the foetal brain: a case of atypical choroid plexus papilloma. *J*  
413 *Obstet Gynaecol* 2017;37(4):525–27.

414 Ferraioli G, Filice C, Castera L, Choi BI, Sporea I, Wilson SR, Cosgrove D, Dietrich CF,  
415 Amy D, Bamber JC, Barr R, Chou YH, Ding H, Farrokh A, Friedrich-Rust M, Hall TJ,  
416 Nakashima K, Nightingale KR, Palmeri ML, Schafer F, Shiina T, Suzuki S, Kudo M.  
417 WFUMB guidelines and recommendations for clinical use of ultrasound elastography:  
418 Part 3: liver. *Ultrasound Med Biol* 2015;41(5):1161–79.

419 Fowlkes JB. American institute of ultrasound in medicine consensus report on potential  
420 bioeffects of diagnostic ultrasound. *J Ultrasound Med* 2008;27(4):503–15.

421 Fruscalzo A, Mazza E, Feltovich H, Schmitz R. Cervical elastography during pregnancy: a  
422 critical review of current approaches with a focus on controversies and limitations. *J Med*  
423 *Ultrason* 2016;43(4):493–504.

424 Gennisson JL, Deffieux T, Fink M, Tanter M. Ultrasound elastography: Principles and  
425 techniques. *Diagn Interv Imaging* 2013;94(5):487–95.

426 Germain MA, Webster WS, Edwards MJ. Hyperthermia as a teratogen: parameters  
427 determining hyperthermia-induced head defects in the rat. *Teratology* 1985;31(2):265–  
428 72.

429 Guibal A, Renosi G, Rode A, Scoazec JY, Guillaud O, Chardon L, Munteanu M, Dumortier J,  
430 Collin F, Lefort T. Shear wave elastography: An accurate technique to stage liver fibrosis  
431 in chronic liver diseases. *Diagn Interv Imaging* 2016;97(1):91–99.

432 Hernandez-Andrade E, Auriolles-Garibay A, Garcia M, Korzeniewski SJ, Schwartz AG, Ahn  
433 H, Matinez-Varea A, Yeo L, Chaiworapongsa T, Hassan SS, Romero R. Effect of depth  
434 on shear-wave elastography estimated in the internal and external cervical os during  
435 pregnancy. *J Perinat Med* 2013;42(5):549–57.

436 Hinoue A, Fushiki S, Nishimura Y, Shiota K. In utero exposure to brief hyperthermia  
437 interferes with the production and migration of neocortical neurons and induces apoptotic  
438 neuronal death in the fetal mouse brain. *Brain Res Dev Brain Res* 2001;132(1):59–67.

439 Issaoui M, Debost-Legrand A, Skerl K, Chauveau B, Magnin B, Delabaere A, Boyer L,  
440 Sauvant-Rochat MP, Lémery D. Shear wave elastography safety in fetus: a quantitative  
441 health risk assessment. *Diagn Interv Imaging* 2018;99(9):519–24.

442 Khalil MR, Thorsen P, Uldbjerg N. Cervical ultrasound elastography may hold potential to  
443 predict risk of preterm birth. *Dan Med J* 2013;60(1):A4570.

444 Kiliç F, Kayadibi Y, Yuksel MA, Adaletli I, Ustabaşoğlu FE, Oncul M, Madazli R, Yılmaz  
445 MH, Mihmanli I, Kantarci F. Shear wave elastography of placenta: in vivo quantitation of  
446 placental elasticity in preeclampsia. *Diagn Interv Radiol* 2015;21(3):202–7.

447 Liang XG, Ge XS, Zhang YP, Wang GJ. A convenient method of measuring the thermal  
448 conductivity of biological tissue. *Phys Med Biol* 1991;36(12):1599–1605.

449 Marinac-Dabic D, Krulewicz CJ, Moore RM Jr. The safety of prenatal ultrasound exposure  
450 in human studies. *Epidemiology* 2002;13 Suppl 3:S19–22.

451 Miloro P, Eleanor M, Adam S. Temperature elevation measured in a tissue-mimicking  
452 phantom for transvaginal ultrasound at clinical settings. *Ultrasound* 2017;25(1):6–15.

453 Molina FS, Gómez LF, Florido J, Padilla MC, Nicolaidis KH. Quantification of cervical  
454 elastography: a reproducibility study. *Ultrasound Obstet Gynecol* 2012;39(6):685–89.

455 Mottet N, Aubry S, Vidal C, Boiteux G, Metz JP, Riethmuller D, Pazart L, Ramanah R.  
456 Feasibility of 2-D ultrasound shear wave elastography of fetal lungs in case of threatened  
457 preterm labour: a study protocol. *BMJ Open* 2017;7(12):e018130.

458 Nitta N, Ishiguro Y, Sasanuma H, Taniguchi N, Akiyama I. Experimental system for in-situ  
459 measurement of temperature rise in animal tissue under exposure to acoustic radiation  
460 force impulse. *J Med Ultrason (2001)* 2015;42(1):39–46.

461 O'Hara S, Zelesco M, Sun Z. Shear wave elastography on the uterine cervix: technical  
462 development for the transvaginal approach. *J Ultrasound Med* 2018;  
463 <https://doi.org/10.1002/jum.14793>

464 Palmeri ML and Nightingale KR. On the thermal effects associated with radiation force  
465 imaging of soft tissue. *IEEE Trans Ultrason Ferroelectr Freq Control* 2004;51(5):551–65.

466 Pellicer B, Herraiz S, Táboas E, Felipo V, Simon C, Pellicer A. Ultrasound bioeffects in rats:  
467 quantification of cellular damage in the fetal liver after pulsed doppler imaging.  
468 *Ultrasound Obstet Gynecol* 2011;37(6):643–48.

469 Quarello E, Lacoste R, Mancini J, Melot–Dusseau S, Gorincour G. Shear wave elastography  
470 of fetal lungs in pregnant baboons. *Diagn Interv Imaging* 2016;97(6):605–10.

471 Schneider-Kolsky ME, Ayobi Z, Lombardo P, Brown D, Kedang B, Gibbs ME. Ultrasound  
472 exposure of the foetal chick brain: effects on learning and memory. *Int J Dev Neurosci*  
473 2009;27(7):677–83.

474 Shankar H and Pagel PS. Potential adverse ultrasound-related biological effects: a critical  
475 review. *Anesthesiology* 2011;115(5):1109–24.

476 Shiina T, Nightingale KR, Palmeri ML, Hall TJ, Bamber JC, Barr RG, Castera L, Choi BI,  
477 Chou YH, Cosgrove D, Dietrich CF, Ding H, Amy D, Farrokh A, Ferraioli G, Filice C,  
478 Friedrich-Rust M15, Nakashima K, Schafer F, Sporea I, Suzuki S, Wilson S, Kudo M.  
479 WFUMB guidelines and recommendations for clinical use of ultrasound elastography:  
480 Part 1: basic principles and terminology. *Ultrasound Med Biol* 2015;41(5):1126–47.

481 Skurczynski MJ, Duck FA, Shipley JA, Bamber JC, Melodelima D. Evaluation of  
482 experimental methods for assessing safety for ultrasound radiation force elastography.  
483 *Brit J Radiol* 2009;82(980):666–74.

484 Tabaru M, Yoshikawa H, Azuma T, Asami R, Hashiba K. Experimental study on temperature  
485 rise of acoustic radiation force elastography. *J Med Ultrason (2001)* 2012;39(3):137–46.

486 Thomas A, Kümmel S, Gemeinhardt O, Fischer T. Real-time sonoelastography of the cervix:  
487 tissue elasticity of the normal and abnormal cervix. *Acad Radiol* 2007;14(2):193–200.

488 Ziskin MC and Morrissey J. Thermal thresholds for teratogenicity, reproduction, and  
489 development. *Int J Hyperthermia* 2011;27(4):374–87.

490

491 **Figure captions list**

492

493 **Fig. 1** Experimental setup: a) two tested configurations, b) schematic views of Configuration  
494 #1, c) photographs of the experiment involving a curved transducer.

495 **Fig. 2.** Illustration of the benefit of using the reference sample. Data correspond here to a test  
496 performed in Configuration #1 for B-mode.

497 **Fig. 3.** Maps of temperature change at  $t = 80$  s for Configuration #1: a) B-mode, b) PD,  
498 c) SWE. The color scale is the same as in Figs. 4-a and -b for comparison purposes.  
499 d) Snapshots of the central zone with suitable color scales.

500 **Fig. 4.** Maps of temperature change at  $t = 360$  s for Configuration #1: a) B-mode, b) PD,  
501 c) SWE.

502 **Fig. 5.** Maps of temperature change at  $t = 360$  s for Configuration #2: a) B-mode, b) PD,  
503 c) SWE.

504 **Fig. 6.** Temperature change at points A and B for a) Configuration #1 and b) Configuration  
505 #2, respectively. The vertical dashed lines correspond to the end of transducer activation.

506 **Fig. 7.** Temperature change at point C for Configuration #2, for comparison purposes with  
507 point A in Configuration #1 (compare with in Fig. 6-a). The vertical dashed line corresponds  
508 to the end of transducer activation. The hatched area corresponds to the part of the sample  
509 which is not present in Configuration #1.

510 **Fig. 8.** B-mode: a) temperature change as a function of time in Configuration #1, b) same in  
511 Configuration #2. The vertical dashed lines correspond to the end of transducer activation.

512 **Fig. 9** Temperature change as a function of time for the Pulse-Doppler mode: a) in  
513 Configuration #1, b) in Configuration #2. Location of the points is the same as in Figs. 8-a  
514 and -b. The vertical dashed lines correspond to the end of transducer activation

515 **Fig. 10** Temperature change as a function of time for the SWE mode: a) in Configuration #1,  
516 b) in Configuration #2. Location of the points is the same as in Figs. 8-a and -b. The vertical  
517 dashed lines correspond to the end of transducer activation

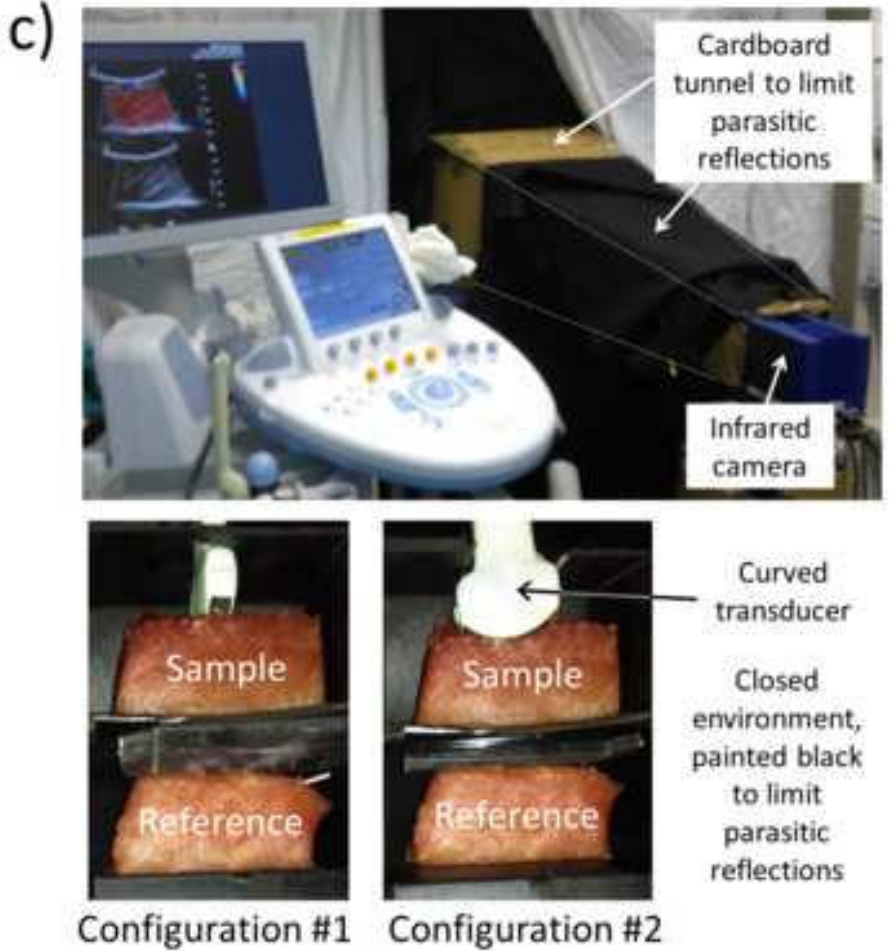
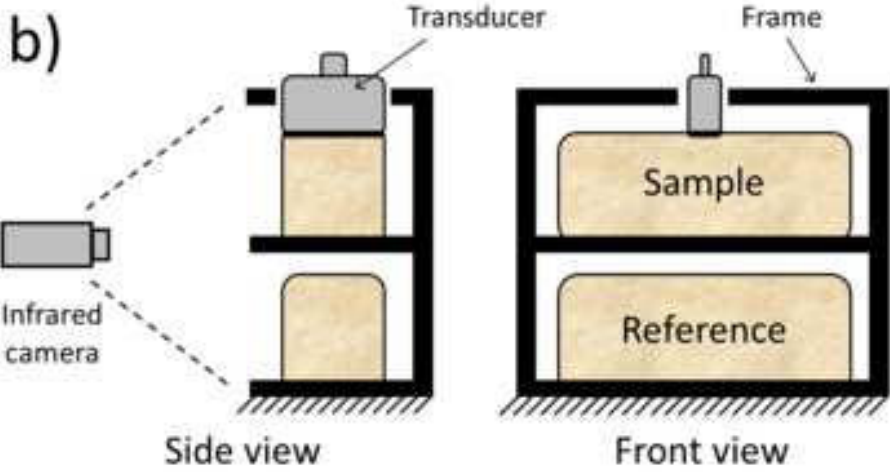
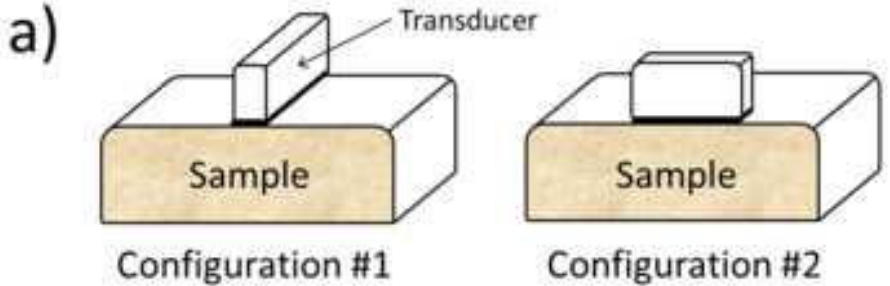




Figure 2

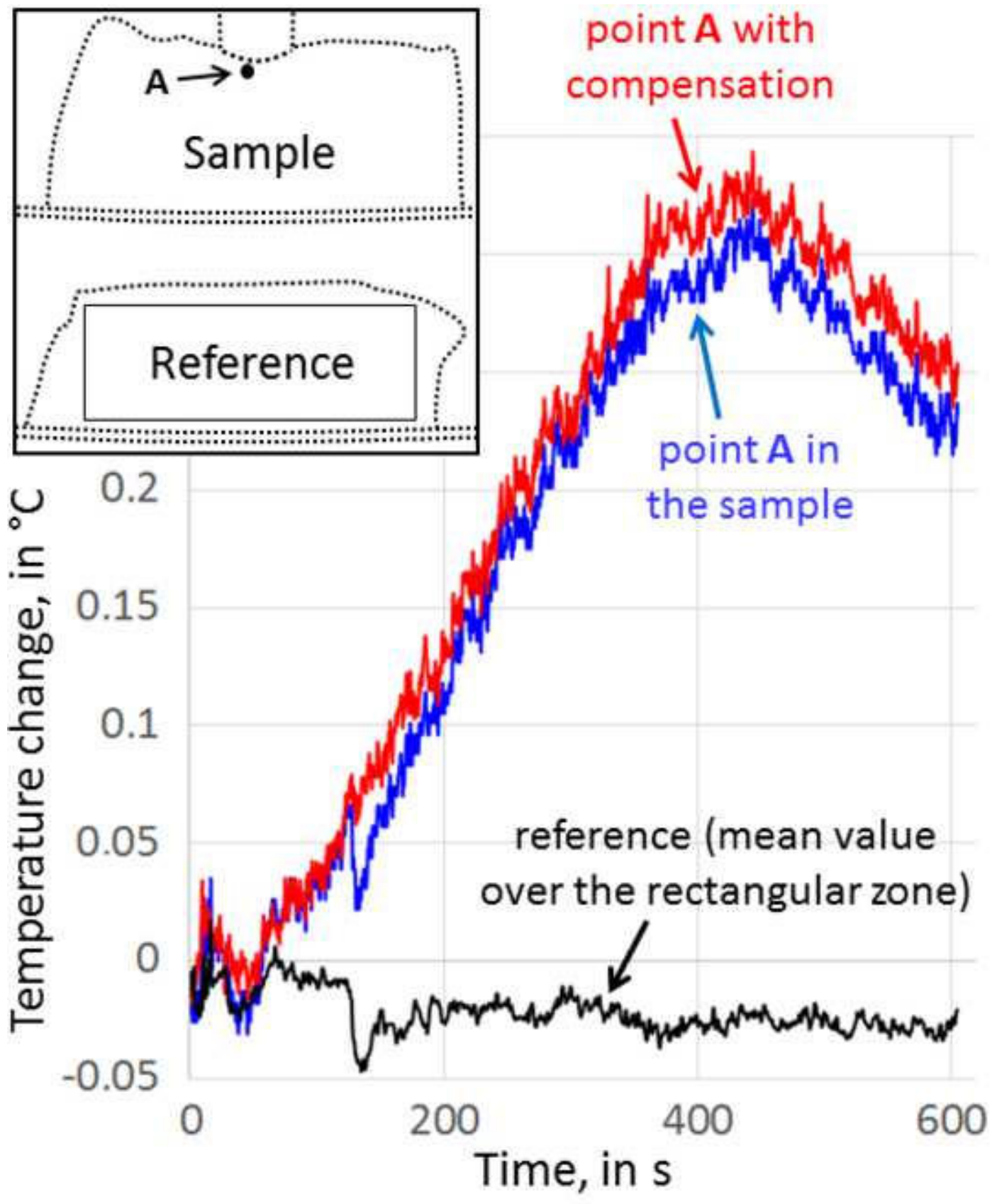


Figure 3

[Click here to download Figure Figure3.tif](#)

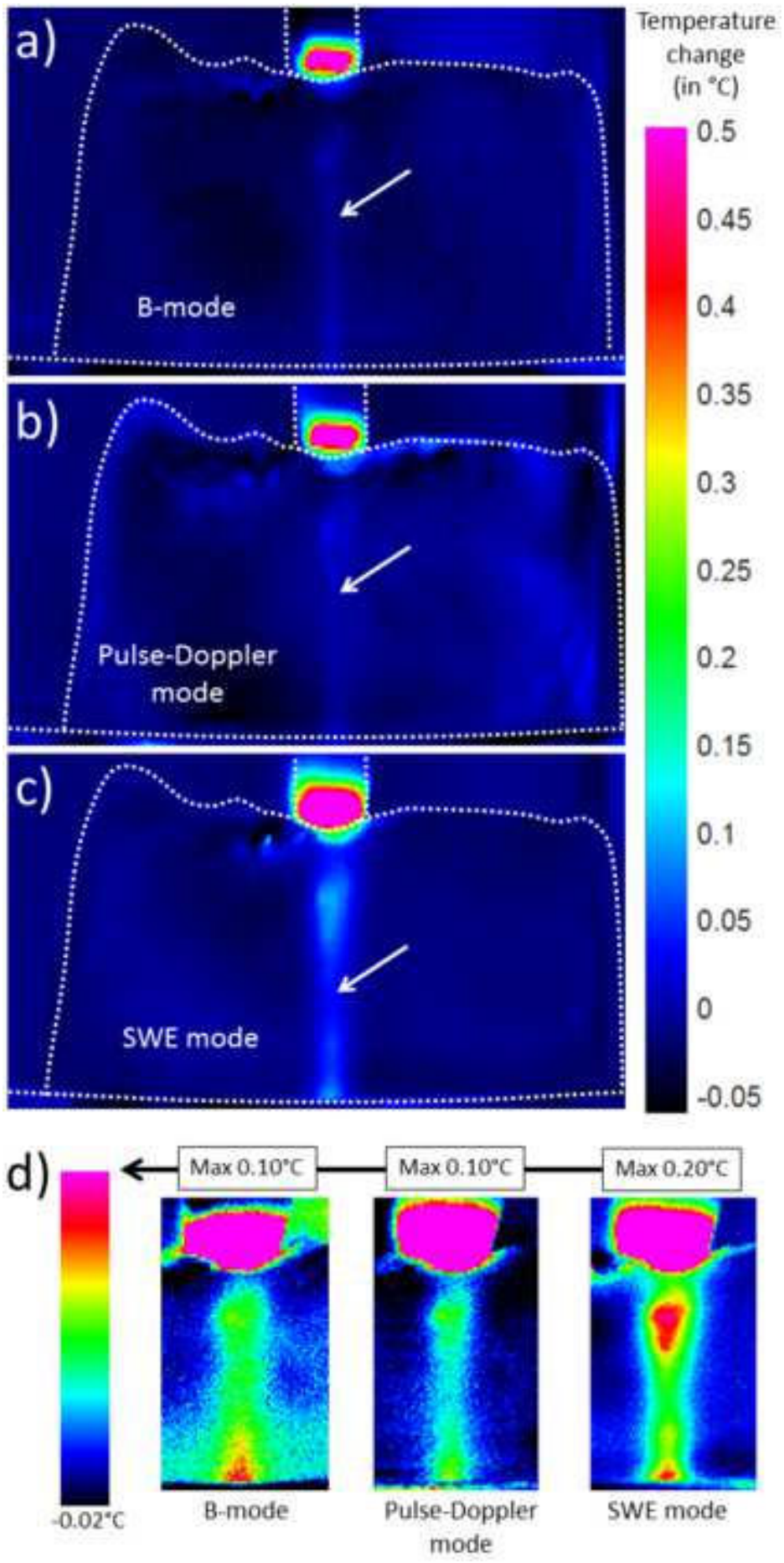


Figure 4

[Click here to download Figure Figure4.tif](#)

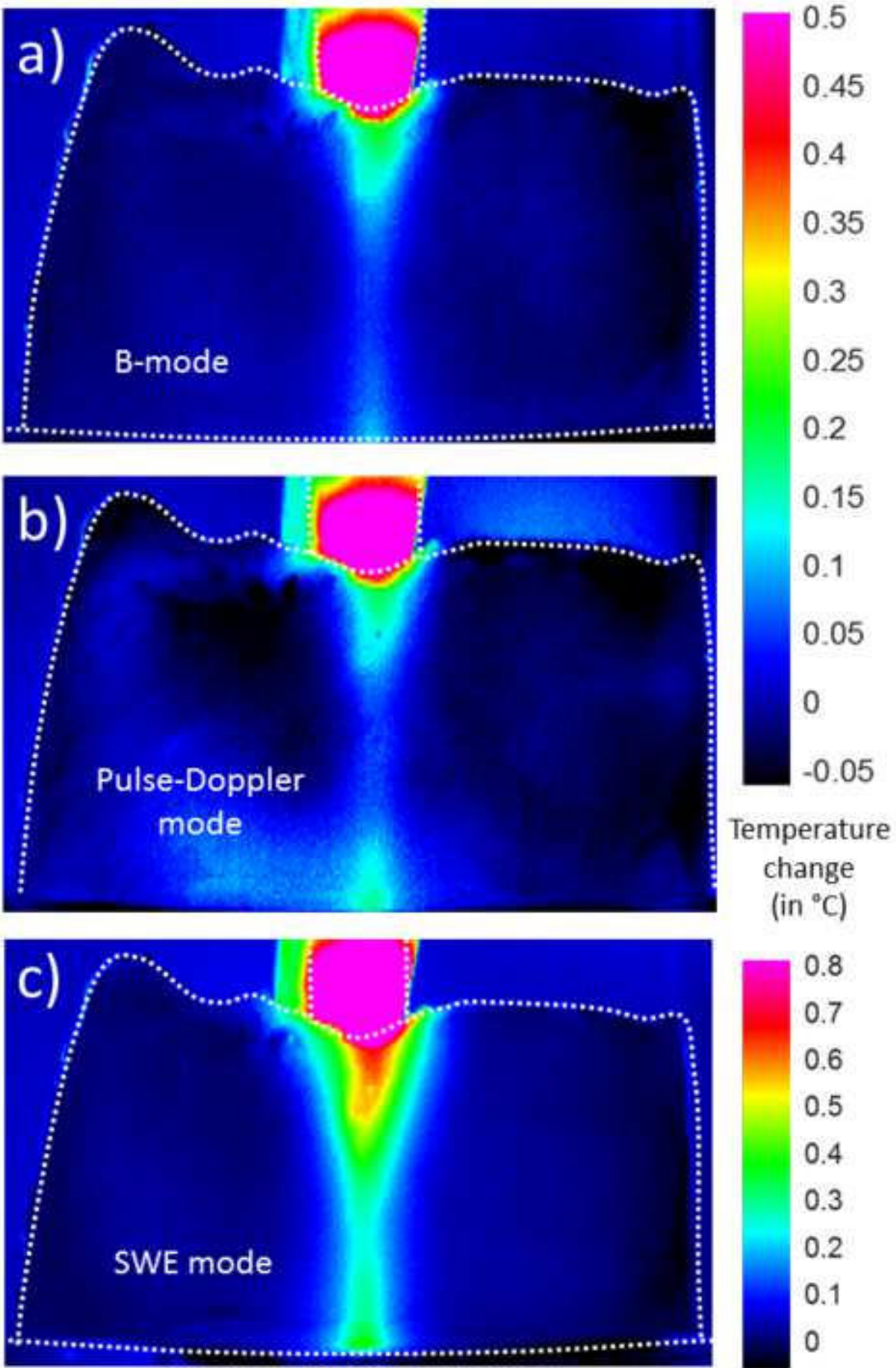
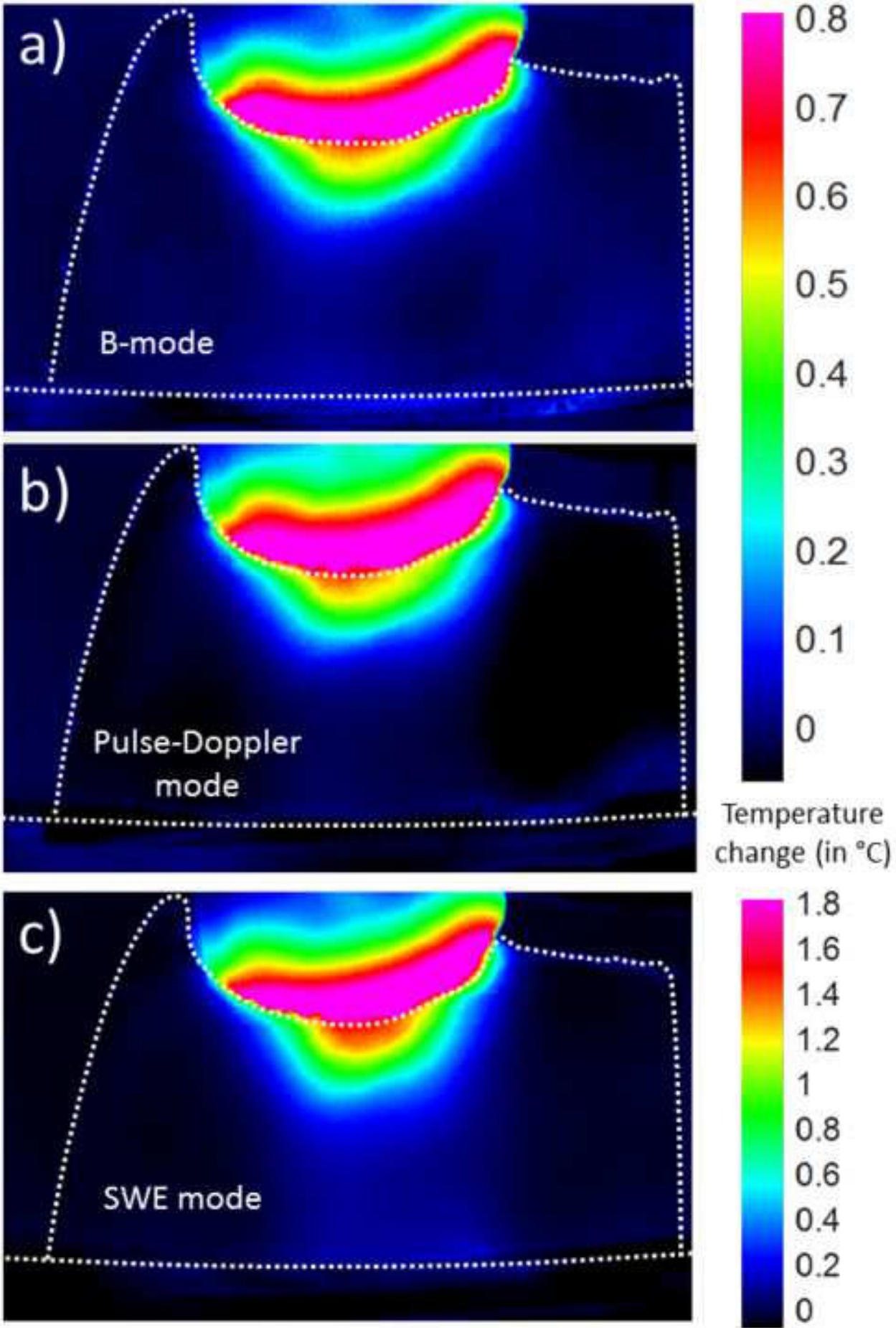
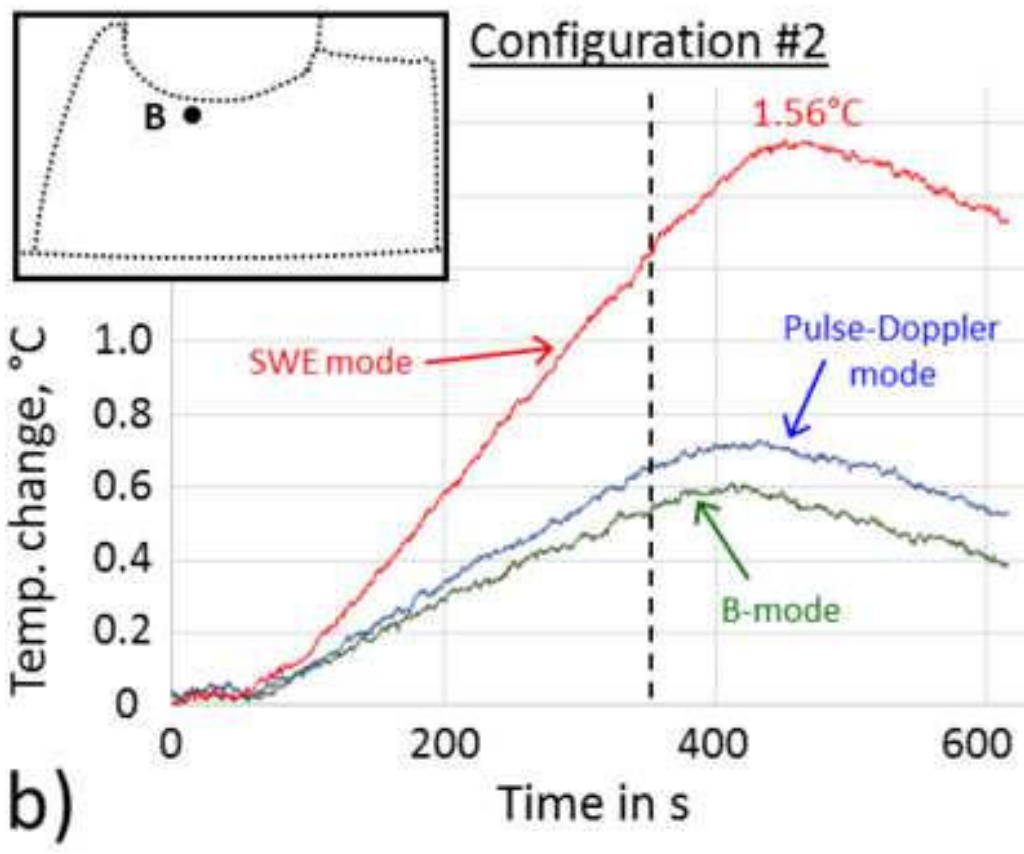
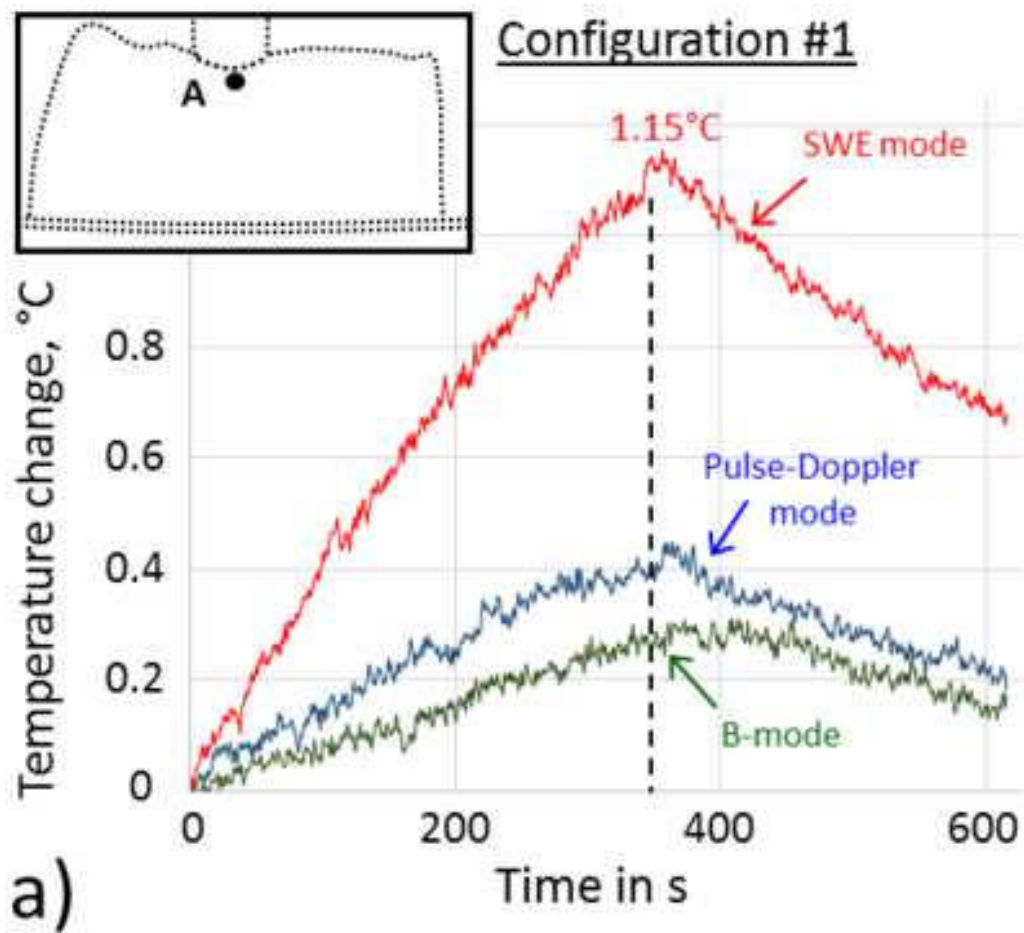
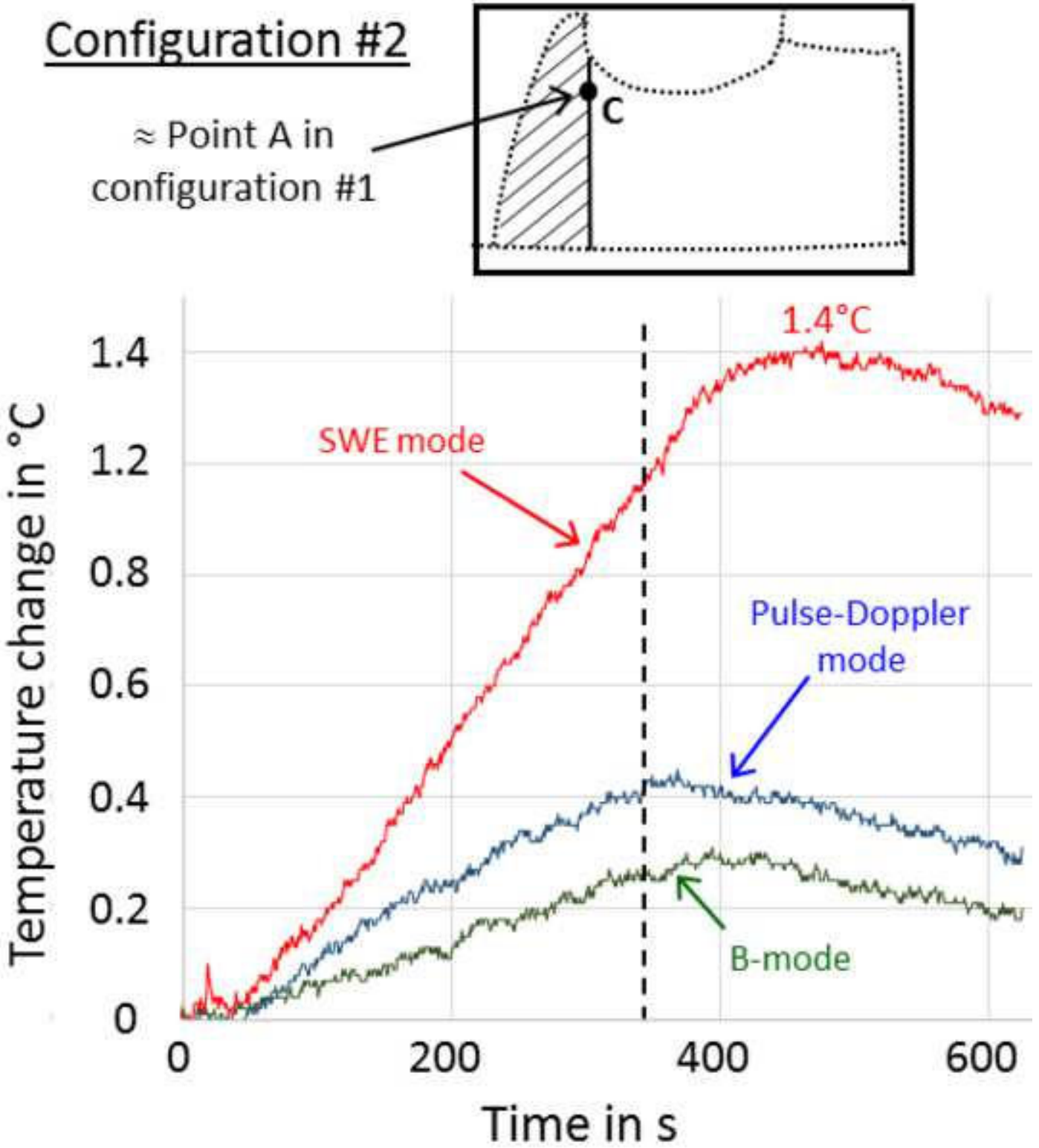


Figure 5

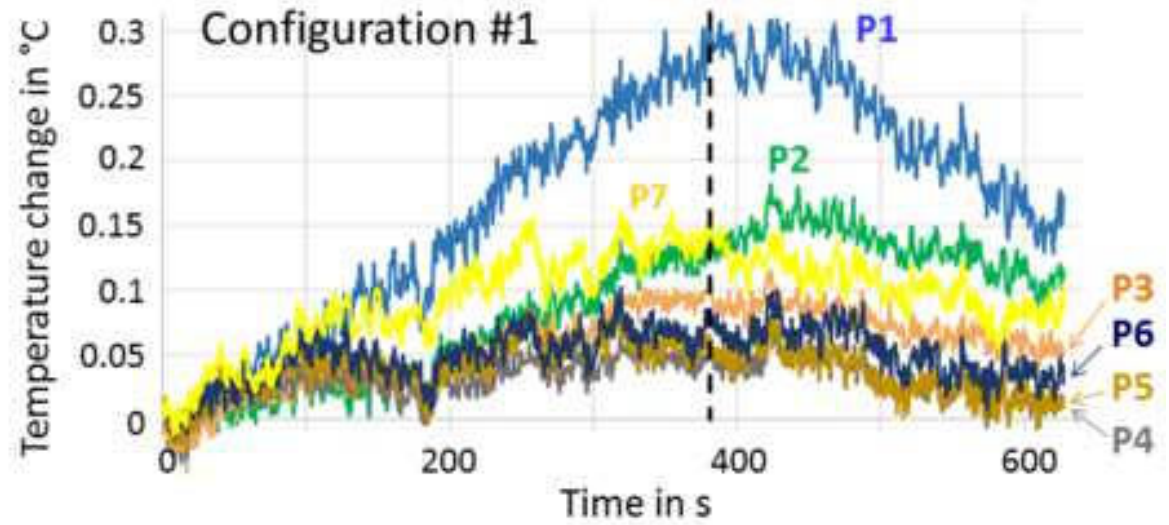
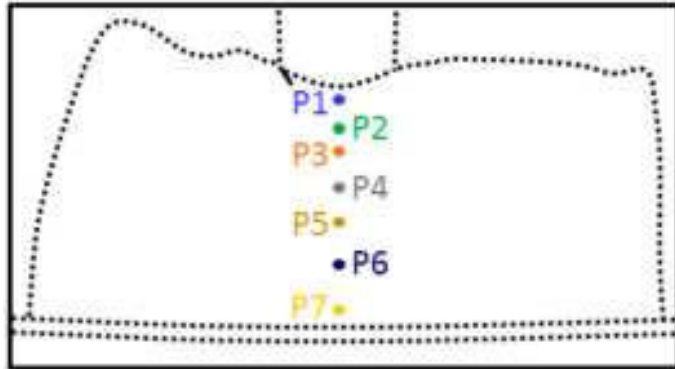
[Click here to download Figure Figure5.tif](#)







a)



b)

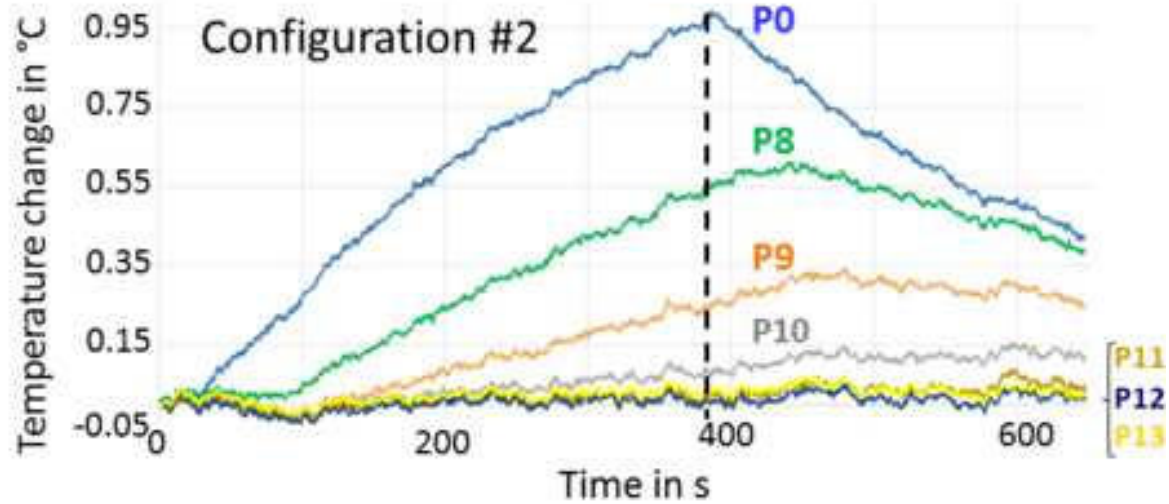
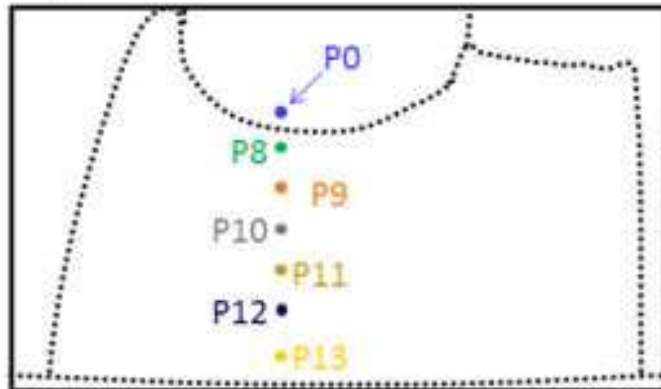
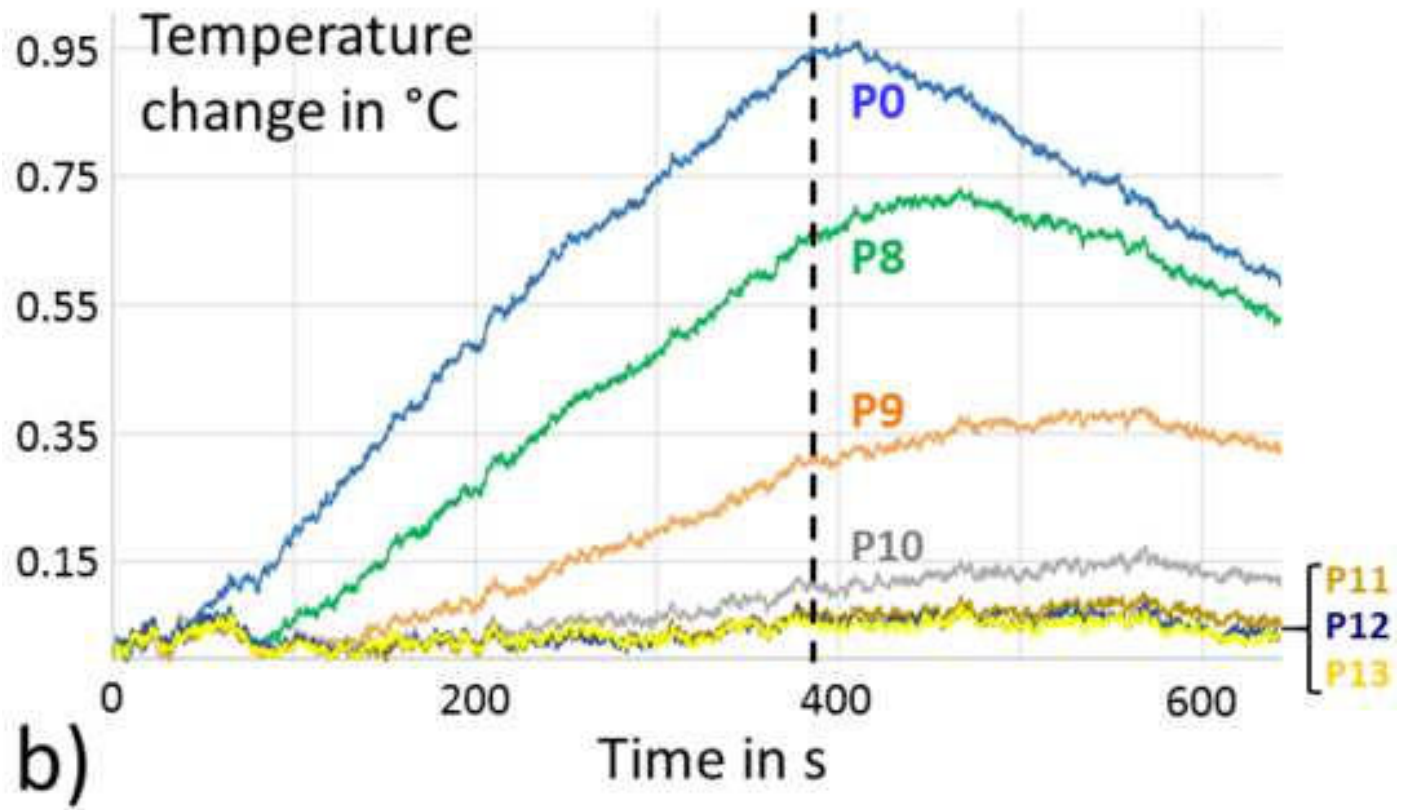
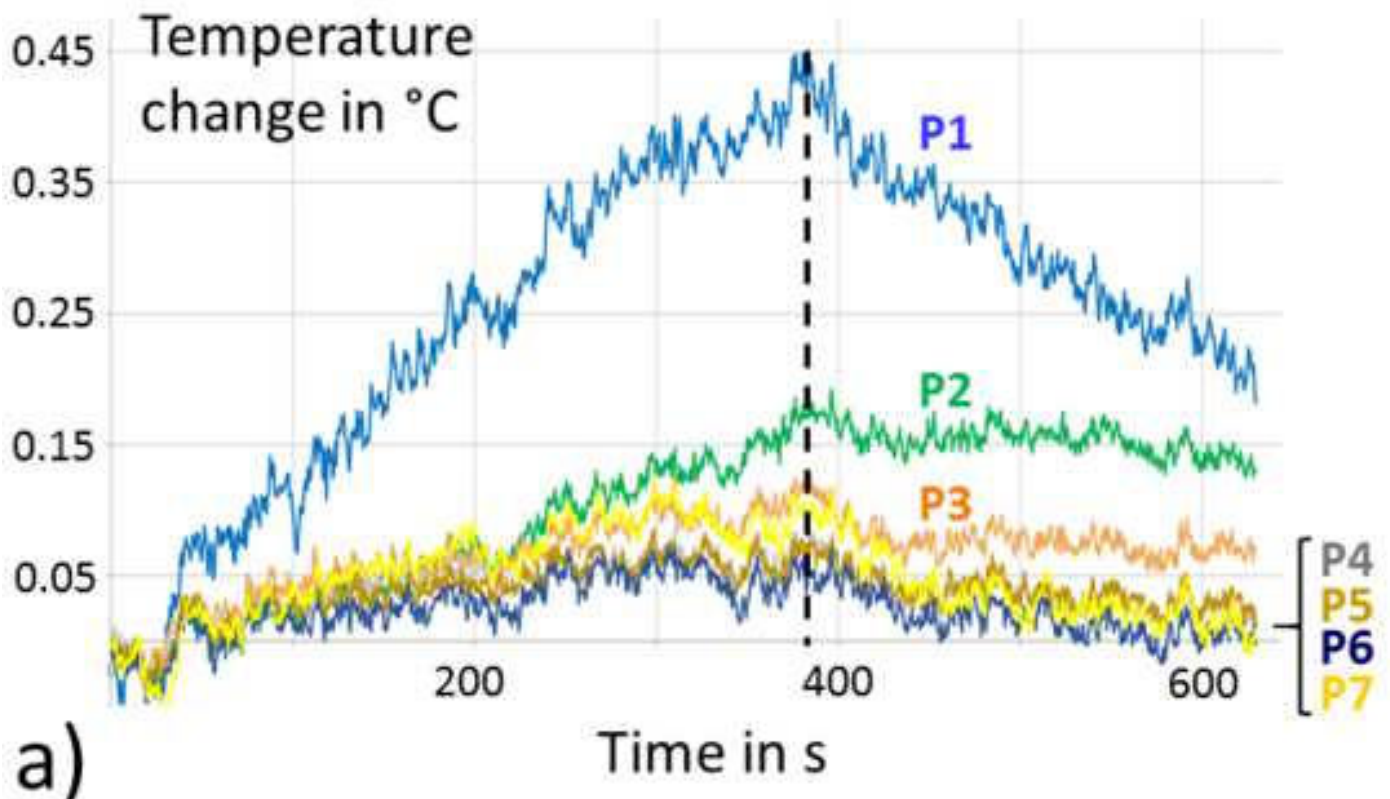
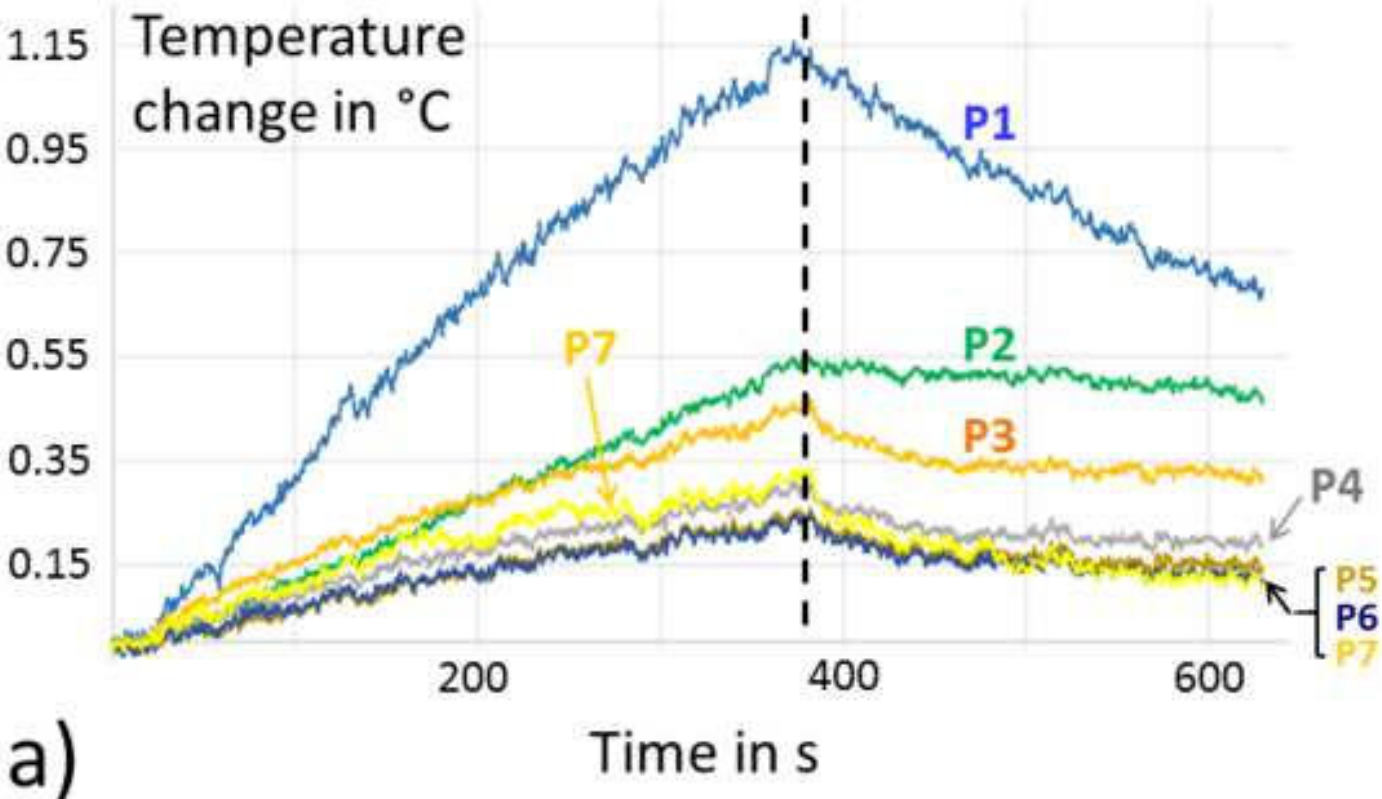


Figure 9

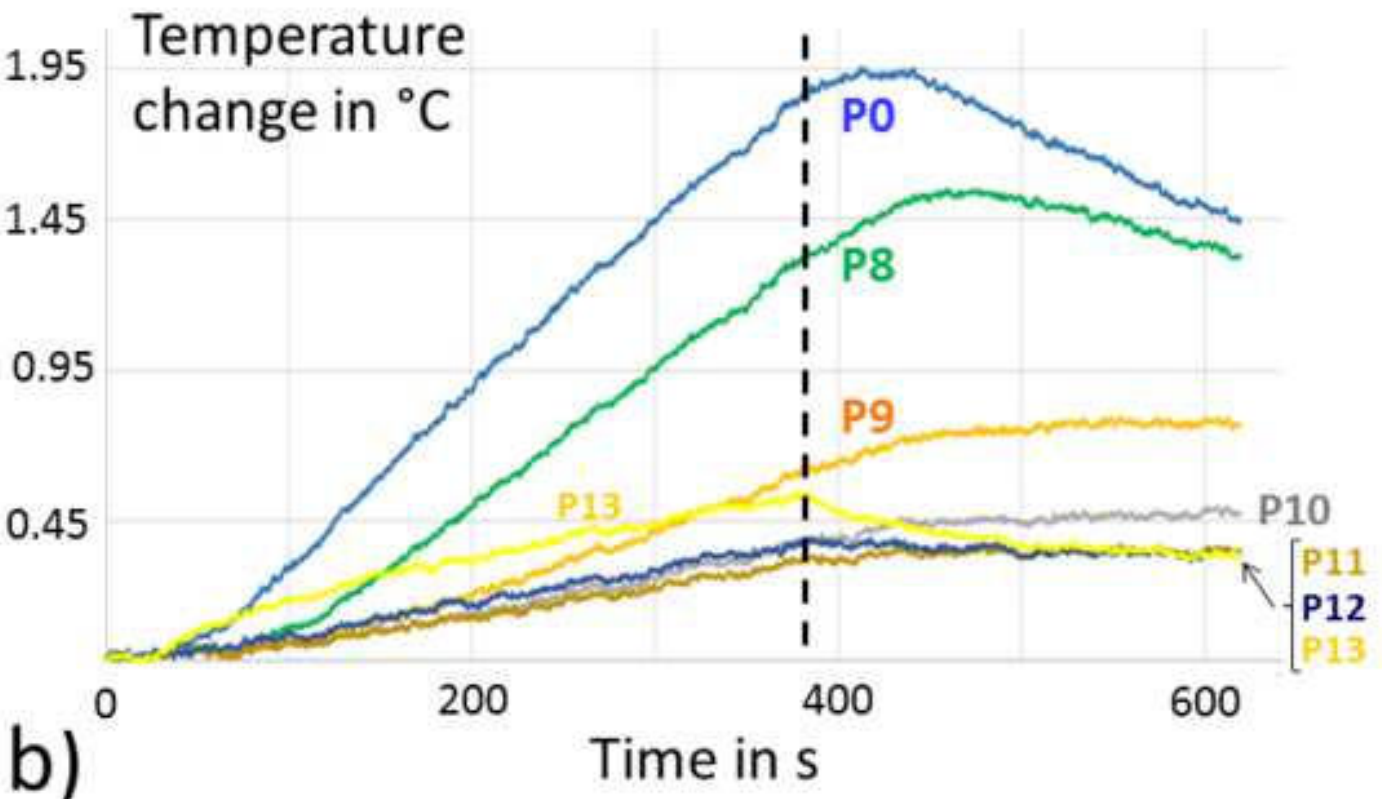
[Click here to download Figure Figure9.tif](#)







a)



b)